nature energy

ARTICLES

https://doi.org/10.1038/s41560-022-01102-w

Check for updates

Efficient monolithic all-perovskite tandem solar modules with small cell-to-module derate

Xuezeng Dai[1], Shangshang Chen[1], Haoyang Jiao[1], Liang Zhao[1], Ke Wang[2], Zhenyi Ni[1], Zhenhua Yu[1], Bo Chen[1], Yongli Gao[2] and Jinsong Huang[1,3] ✉

All-perovskite tandem solar modules are promising to reduce the cost of photovoltaic systems with their high efficiency and solution fabrication, but their sensitivity to air still imposes a great challenge. Here a hot gas-assisted blading method is developed to accelerate the perovskite solidification, forming compact and thick narrow bandgap (NBG) perovskite films. Adding a reduction agent into NBG films followed by a short period of air exposure and a post-fabrication storage surprisingly increases carrier recombination lifetime and enables laser scribing in ambient conditions without obvious loss of device performance. This combination suppresses tin and iodide oxidation and forms a thin SnO_2 layer on the NBG film surface. Monolithic all-perovskite tandem solar modules showed a champion efficiency of 21.6% with a 14.3 cm^2 aperture area, corresponding to an active area efficiency of 23.0%. The very small cell-to-module derate of 6.5% demonstrates the advantage of a tandem monolithic structure for solar modules.

Tandem perovskite solar cells have cut a fine figure in the rapid development of perovskite photovoltaic techniques due to their potential to reach a much higher efficiency than the detailed balanced efficiency limit of single-junction solar cells, which may contribute to a reduction of cost of photovoltaic systems[1]. Compared with single-junction perovskite modules, the application tandem structure, which has much smaller photocurrent but higher photovoltage, can also reduce the cell-to-module efficiency derate[2] and thus realize higher module efficiency for monolithically interconnected modules in series. After addressing the issues associated with the low diffusion length in tin-containing Sn–Pb perovskites, the efficiency of all-perovskite tandem cells quickly rose from 10.4% (ref. [3]) to 26.4% (ref. [4]), which already surpassed that of single-junction perovskite cells[5]. However, compared with the fast progress made on scaling up the single-junction perovskite modules in recent years, the upscaling of all-perovskite tandem modules is lagging behind mainly due to the challenges for the narrow bandgap (NBG) perovskite process in ambient conditions.

We identified the module-level fabrication of NBG perovskites and the subsequent laser scribing in air to be the bottlenecks that hinder the development of all-perovskite tandem solar modules. For lead-based perovskites, we have successfully developed the gas-assisted blade-coating method to fabricate large-area single-junction perovskite modules with record efficiencies[6–10]. To coat highly crystalline and compact films at high throughput, volatile solvents such as 2-methoxyethanol (boiling point of 124 °C) and acetonitrile (boiling point of 82 °C) were used to accelerate solvent evaporation during scalable coating[6–10]. However, such solvents do not dissolve Cs-, Br- or Sn-based precursors well; those are needed to fabricate more efficient and stable wide bandgap (WBG) and NBG perovskite cells. Instead, common solvents such as dimethylformamide (DMF, boiling point of 153 °C) and dimethyl sulfoxide (DMSO, boiling point of 189 °C) are still the best for the WBG and NBG perovskite precursors. These non-volatile solvents do not easily escape from the as-coated wet films even with the help of high-flow rate gas, mainly due to their high boiling points and strong coordination to Pb^{2+} ions[9]. This challenge is even more severe in NBG perovskites because its optimal thickness is generally larger than that in single-junction perovskite devices, induced by the low absorption coefficient of Sn–Pb perovskites in near-infrared range[11,12]. Raising film annealing temperature cannot solve this problem because the flowing of the precursor solution in a wet film right after coating drives the formation of large domains and non-continuous films[13]. Consequently, it is much more challenging to deposit large-area, compact and smooth NBG perovskite films using a scalable fabrication process.

Another obstacle is the oxidation of NBG perovskites due to air exposure in the following device-fabrication process steps after film deposition, including deposition of charge transport layers and laser scribing for module fabrication. Sn^{2+} in NBG perovskites can be readily oxidized to Sn^{4+}, which generates defects and excess doping of NBG perovskites and thus reduces device efficiency. To this end, reducing agents have been reported to prevent the oxidation of Sn^{2+}, including metal Sn[14,15], hydrazine[16,17] and other Lewis bases[12,18–20]. However, most of them are aimed at removing Sn^{4+} in the precursor solution or during film deposition. The oxidation of Sn^{2+} during processes such as laser scribing for module fabrication has not been investigated. Laser scribing is an essential step to create monolithic interconnected modules. It is often conducted in air, exposing perovskites and scribed area to air[21].

Here we report the scalable fabrication of perovskite tandem modules by blade coating. A hot gas-assisted blade-coating system was developed to fabricate high-quality and thick NBG perovskite films. The hot gas accelerated the drying of the high boiling point solvents to solidify the as-coated film, preventing the microscale solution flows. In addition, a reducing agent benzylhydrazine hydrochloride (BHC) was introduced to prevent Sn^{2+} oxidation during film deposition and, more importantly, to withstand the air exposure during laser scribing. Surprisingly, air exposure of NBG perovskite films for a few minutes actually boosted the power conversion

[1]Department of Applied Physical Sciences, University of North Carolina at Chapel Hill, Chapel Hill, NC, USA. [2]Department of Physics and Astronomy, University of Rochester, Rochester, NY, USA. [3]Department of Chemistry, University of North Carolina at Chapel Hill, Chapel Hill, NC, USA. ✉e-mail: jhuang@unc.edu

efficiency (PCE) of NBG cells, resulting from the generation of *n*-type SnO_2 on the surface and the reduction of detrimental Sn^{4+} and iodine by BHC during storage. This phenomenon enables completion of the module fabrication in air and resulted in an aperture PCE of 21.6% for the all-perovskite tandem mini module with an area of 14.3 cm^2, surpassing that of single-junction perovskite mini modules. The cell-to-module derate is only 6.5%, which is around one-third of the cell-to-module loss in single-junction modules.

Blade coating high-quality NBG films

The NBG perovskite composition in this study is $Cs_{0.2}FA_{0.8}Pb_{0.5}Sn_{0.5}I_3$ which has a bandgap of 1.22 eV. The optimal thickness of this NBG perovskite for tandem devices was reported to be 1,000 nm (ref. [11]). To fabricate such thick films by blade coating, the as-coated wet films also need to be thick enough, given that the NBG solution precursor concentration is not higher than that of lead perovskites. Figure 1 shows our blading system setup, photos of the films coated under different conditions and scanning electron microscopy (SEM) images of the perovskite films annealed after different durations. In our initial trials, we applied our well-established room temperature (RT, 20 ± 1 °C) N_2-assisted blade-coating method to coat the 1,000 nm thick NBG films[6–9]. However, the DMF/DMSO-based precursor solution dried much slower so that a large amount of precursor solution remained in the coated film (Fig. 1c). Post-annealing of such films at 100 °C drove the precursor solution to flow, leaving non-continuous perovskite films with gaps between large domains, as shown in the SEM images in Fig. 1c and Supplementary Fig. 1. Such a domain structure growth has been observed in our previous study where the slow-drying ink was blade coated on heated substrates[13]. The flowing of precursor solution towards early nucleation sites forms such domain structures (not single crystalline). The domains were found to form within 1 s of annealing, and additional annealing did not change the domain structure anymore (Fig. 1c; 3 s–420 s). To address this issue, we accelerated the solvent evaporation during blading by raising the N_2 temperature. Hot air-assisted drying was applied in spin coating[22], spray coating[23] and slot die coating[24] of perovskites that are less sensitive to air. However, in those studies, hot air from hot guns had limited control of gas temperature and flow rate and could treat only small area films (< 1 cm^2). The hot gas system developed by us has an in-line heater (Omega, AHPF-121) that transports heated gas to a wide gas knife (15 cm) to provide precise control of gas temperature and flow rate. To avoid oxidation of Sn perovskites, nitrogen was used as the working gas and was heated to 40 °C, 70 °C and 100 °C. The blade-coated film pictures and their SEM images are shown in Fig. 1d–f. With 40 °C N_2, the as-coated film showed a grey colour, a sign of more efficient solvent removal during blading. However, the domain pattern still existed, though it became smaller. When N_2 temperature was elevated to 70 °C, the film showed a light black colour without annealing, indicating most solvents had already evaporated. However, large pinholes were still observed in the whole film despite no domain pattern being captured after the annealing. Eventually, 100 °C N_2 created a dark black film right after blading. X-ray diffraction (XRD) results in Supplementary Fig. 2 revealed that the as-coated film was already converted to the perovskite phase right after blading. SEM images (Fig. 1f) confirmed the formation of pinhole-free, compact perovskite films after annealing. The rapid solvent extraction assisted by hot gas quickly formed solid films, which prevents the particles from moving during thermal annealing. The anti-solvent bathing[25–27] is an alternative strategy to quickly remove the precursor solvents from films. However, such a strategy requires a relatively long bathing time, and there is also a strict requirement of bathing solvent. Superior to the anti-solvent method, the hot gas strategy is a physical approach that avoids using any solvent, making it much easier to integrate into the high-speed sheet-to-sheet or roll-to-roll manufacturing production lines. We also looked into whether tiny extra strain was introduced into the films by hot gas drying. As shown by the XRD patterns in Supplementary Fig. 3, there was no lattice constant change for the films made by hot gas drying. This can be explained by the following grain-growth process during annealing releasing the possible strain in the perovskite films. We also evaluated the feasibility of coating NBG perovskite films using pre-heated substrates, and the discussion can be found in Supplementary Note 1, showing that using hot gas is a superior strategy for fabricating high-quality thick NBG perovskite films.

The generation of voids at the perovskite–substrate interfaces in bladed thick perovskites was previously observed; they are caused by the evaporation of trapped DMSO near the bottom of the perovskite films and downward growth of perovskite films due to initial evaporation of solvents from the top surface[28,29]. Such voids could dramatically reduce device performance[10,28]. To find out whether these thick NBG perovskite films have voids, we conducted cross-section SEM measurement. The SEM images shown in Fig. 1g uncovered many voids generated at the bottom of the perovskite films made with 100 °C hot gas-assisted blading when DMSO/(Pb + Sn) molar ratio is 16%. To prevent the formation of the voids, we reduced the DMSO/(Pb + Sn) molar ratio to 8% and 4%. As shown in Fig. 1h, the 8% DMSO resulted in the formation of void-free films with large monolithic grains. However, 4% DMSO generated films with multi-layer small grains (Fig. 1i) that contain more grain boundaries and thus more defects. By tuning the hot gas temperature and DMSO content in the precursor solution, we have successfully fabricated compact NBG perovskites over a large area using a scalable coating process. A high-quality blade-coated large-area NBG perovskite film is shown in Fig. 1b.

Improving NBG device performance by BHC

Suppressing the oxidation of Sn^{2+} in NBG perovskite in air is critical to achieve high performance devices. Therefore, we introduced a reductant BHC into the NBG film. Inspired by the excellent reduction function on preventing the generation of I_2 in iodide perovskites[7], we expect that BHC has the same function of reducing iodine generated during the operation of NBG perovskites. In addition, we verified its capability of reducing Sn^{4+} to Sn^{2+}. A yellow NBG perovskite precursor solution was oxidized in the air until it turned into red, indicating the formation of a large amount of Sn^{4+} in solution[16,30]. As shown in Fig. 2a, after the BHC was added into the oxidized solution, the solution turned back into a yellow colour within 10 s, proving the capability of BHC to reduce Sn^{4+} to Sn^{2+} at room temperature. The product of BHC after the reducing reaction is phenyldiazomethane (Supplementary Scheme 1), which did not obviously harm the NBG perovskites within our testing time range.

We fabricated single-junction devices to evaluate the effect of BHC on NBG solar cell efficiency. The NBG single-junction perovskite solar cells had a structure of glass/indium tin oxide (ITO)/poly(3,4-ethylenedioxythiophene):poly(styrene sulfonate) (PEDOT:PSS)/$Cs_{0.2}FA_{0.8}$ $Pb_{0.5}Sn_{0.5}I_3$/[6,6]-phenyl-C61-butyric acid methyl ester (PCBM)/fullerene (C_{60})/bathocuproine (BCP)/copper (Cu). As the perovskite film surface is most vulnerable to oxidation, we treated the as-coated NBG perovskite surface using BHC dissolved in an orthogonal solvent of 2-propanol with a low concentration of 1 $g\,l^{-1}$. Figure 2b (Supplementary Table 1) shows that BHC surface treatment clearly enhanced the efficiency of NBG solar cells. The open-circuit voltage (V_{OC}) increased from 0.765 V to 0.809 V, and the PCE went up from 17.0% to 18.6%. The enhancement of short-circuit current (J_{SC}) by BHC agrees with the higher external quantum efficiency (EQE) shown in Supplementary Fig. 5. The severe hysteresis disappeared after surface treatment. We further added 0.4 $g\,l^{-1}$ BHC into the precursor solution as an additive with an intention to reduce the pre-existing Sn^{4+} in raw precursor materials and the generated Sn^{4+} during film fabrication processes.

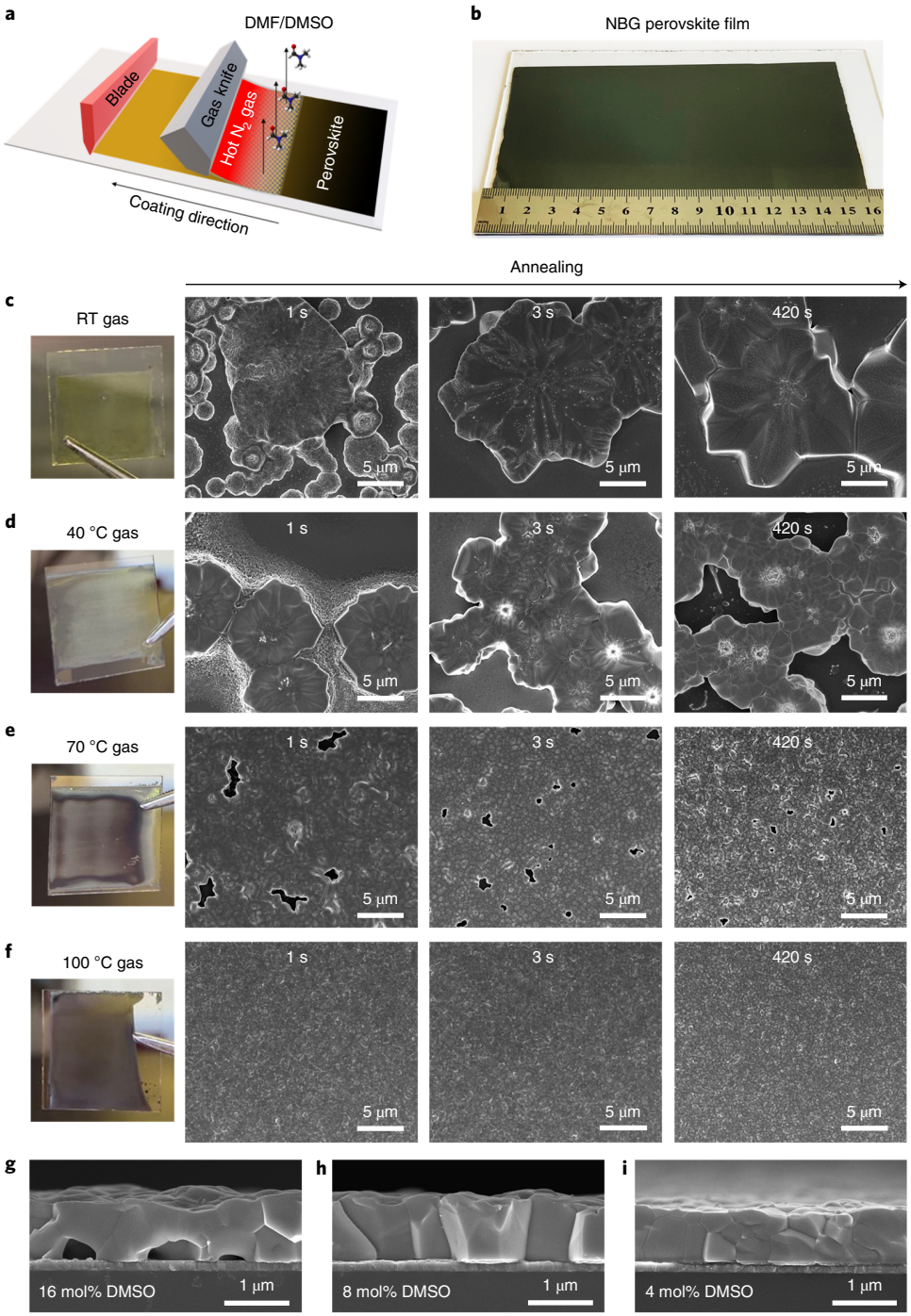

Fig. 1 | Blade coating 1,000 nm thick NBG perovskite films. a, Schematic of hot gas-assisted blade coating. **b**, Picture of a blade-coated NBG perovskite film with dimensions of 16 cm × 9 cm. **c**–**f**, Pictures and SEM images of blade-coated NBG films with gas temperatures at room temperature (c), 40 °C (d), 70 °C (e) and 100 °C (f). First column: pictures before annealing; second to fourth columns: SEM images after 1 s, 3 s and 420 s annealing, respectively. **g**–**i**, Cross-section SEM images of blade-coated NBG films with 16 mol% (g), 8 mol% (h) and 4 mol% (i) DMSO/(Pb + Sn) ratios in the precursor solution.

This further boosted the device V_{OC} to 0.837 V, resulting in a PCE of 19.4% for single-junction NBG perovskite solar cells. We also tested the effectiveness of the other hydrazine halides, and BHC remained to be the best reductant and is also much cheaper than others (Supplementary Note 2). The photo stability of encapsulated NBG perovskite solar cells was measured in air with a relative humidity (RH) of 30–65%. As shown in Supplementary Fig. 7, the cell retained 93.7% of its initial PCE after being soaked under 1 sun light for ~250 h.

Air exposure enhancing NBG device performance

When we fabricated NBG modules that needed a laser scribing process in air, a major concern arose whether the NBG perovskite films could withstand air exposure for a few minutes. To investigate the impact of air exposure, we fabricated small area devices and exposed them to ambient air (20 ± 1 °C, 65 ± 5 RH%) for 1 min, 5 min and 15 min, respectively, before depositing the C_{60}. As shown in Fig. 2c and Table 1, when the devices were measured right after the top electrode deposition, the device with 1 min air exposure

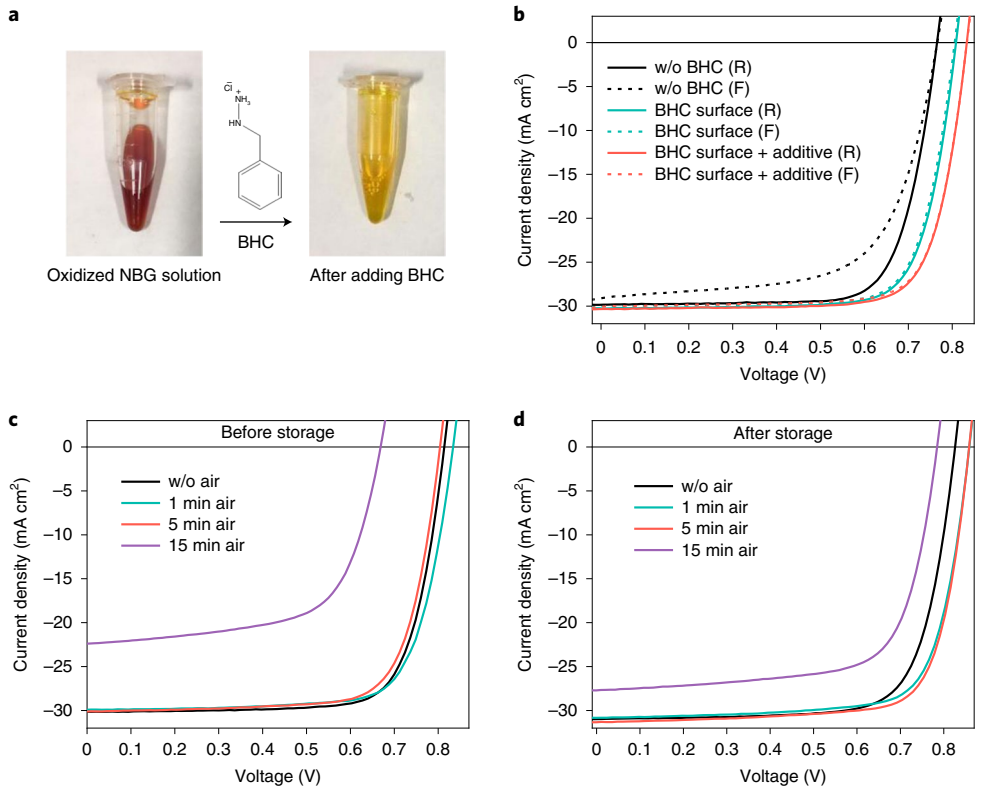

Fig. 2 | Single-junction NBG solar cell performance. a, Pictures of the oxidized NBG precursor solution and reduced solution by BHC. **b**, *J*–*V* curves of single-junction NBG cells with and without (w/o) BHC and with different BHC treatments under forward (F) and reverse (R) scans. **c**,**d**, *J*–*V* curves of BHC-treated single-junction NBG cells with air exposure for 0 min, 1 min, 5 min and 15 min before the deposition of C_{60}; devices were tested before storage (c) and after storage (d) in the glovebox for two days.

Table 1 | Performance summary of BHC-treated single-junction NBG solar cells with air exposure

		V_{OC} (V)	J_{SC} (mA cm^{-2})	Fill factor (%)	PCE (%)
Before storage	Without air	0.814	30.1	75.6	18.5
	1 min air	0.834	29.9	74.6	18.6
	5 min air	0.804	30.1	74.0	17.9
	15 min air	0.669	22.0	63.8	9.4
After storage	Without air	0.826	31.0	74.4	19.1
	1 min air	0.859	30.5	74.9	19.6
	5 min air	0.859	31.3	75.6	20.3
	15 min air	0.785	27.7	70.0	15.2

The air exposure was conducted for 0 min, 1 min, 5 min and 15 min, respectively, before the deposition of C_{60}. The devices were measured before and after storage in the glovebox for two days.

maintained the efficiency of 18.6%. But the more prolonged air exposure to 5 min reduced PCE to 17.9%, as expected; 15 min air exposure dramatically damaged the NBG perovskites, leading to a low PCE of 9.4%.

A surprising phenomenon was observed when we studied the aged NBG device performance, that is, we measured the device efficiencies after storing the devices in the glovebox for a few days. After two days of storage, all devices showed increased efficiency (Fig. 2d and Table 1). Ageing-related efficiency enhancements from Pb perovskite solar cells were reported previously, which were attributed to several different mechanisms including strain relaxation[31,32], defect self-annihilation[33–36] or de-doping[8] of perovskites. However, different from Pb perovskite solar cells, Sn–Pb perovskite devices showed the best efficiency gain by a combination of air exposure of perovskite films during fabrication and ageing of perovskite devices after fabrication. The devices with air-exposed films for 1 min and 5 min had efficiencies of 19.6% and 20.3%, respectively, which are much higher than that of the device without air exposure and comparable to the best spin coated NBG perovskite solar cells[11,12,37]. Even for the severely damaged device after 15 min air exposure, ageing recovered its V_{OC} by 0.116 V and almost doubled its efficiency from 9.4% to 15.2%. We speculate this phenomenon is caused by the BHC additive. To verify it, the same air-exposure tests were conducted on devices without BHC. As shown in Supplementary Fig. 8 and Supplementary Table 2, air exposure of NBG films without BHC caused a quick device degradation, and the ageing process did not recover the efficiencies. These results concluded that the reducing agent BHC played a vital role here.

We examined several hypotheses that may explain the performance enhancement of the device with air exposure after storage. In Supplementary Note 3, we confirmed that oxygen rather than moisture in the air is the key factor in the reaction, and we excluded the redistribution of the excessive amount of doping from the surface to the whole film as the main reason. Then, we scrutinized the oxidation pathway of the tin perovskites. The reported tin perovskite degradation in air follows the reaction[38,39]:

$$2ASnI_3 + O_2 \rightarrow 2AI + SnI_4 + SnO_2 \quad (1)$$

where *A* is MA, FA or Cs. The oxidation of Sn^{2+} to Sn^{4+} is accompanied by the generation of tin vacancies, leading to the *p*-doping and higher non-radiative charge recombination rate[40]. The generated

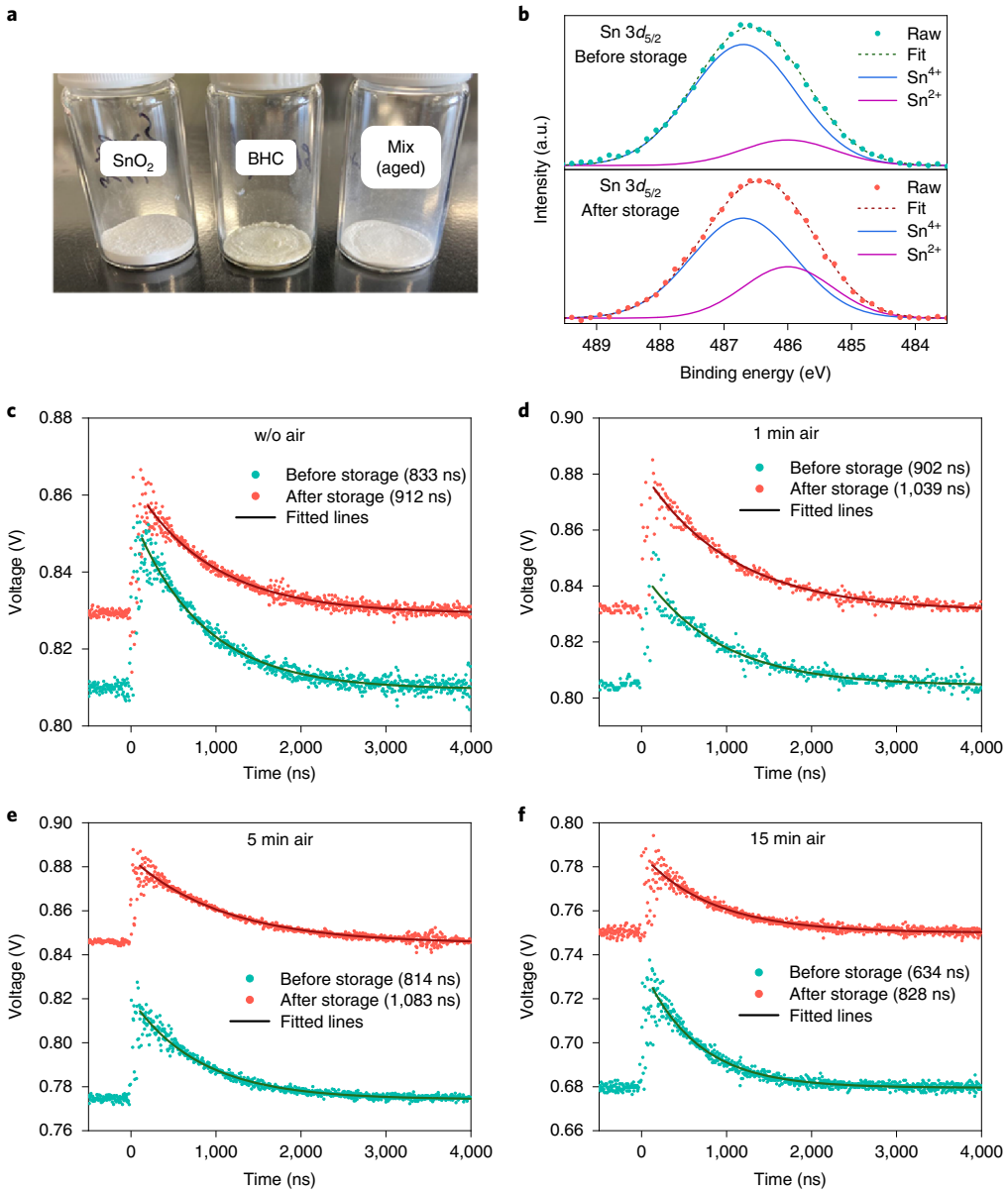

Fig. 3 | Unveiling the mechanism of performance enhancement by air exposure and storage. a, Picture of SnO_2, BHC and SnO_2/BHC mixture milled and stored in the glovebox for ten days. **b**, Measured XPS data (dots) and Gaussian fit (short dashes) of Sn $3d_{5/2}$ peaks for a 15 min air exposure-treated NBG perovskite film before and after storage in the glovebox for two days. **c**–**f**, Carrier recombination lifetimes with exponential fit lines on NBG perovskite solar cells with various perovskite film treatments: without air exposure (c), air exposed for 1 min (d), air exposed for 5 min (e) and air exposed for 15 min (f). The devices were measured before and after storage in the glovebox for two days.

Sn^{4+} exists as SnI_4 and SnO_2. Meanwhile, SnI_4 can convert to SnO_2 and iodine at room temperature with the presence of moisture and oxygen[38]. As shown in Supplementary Note 4, we experimentally verified these reaction products of SnI_4, SnO_2 and iodine in the NBG perovskite after being oxidized in air. We have reported that the detrimental iodine generated in iodide perovskite can be effectively reduced by BHC[7]. In addition, as demonstrated in Fig. 2a, SnI_4 can also be reduced by BHC, whereas the SnO_2, whose Sn–O bond length of 2.13 Å is much shorter than the Sn–I bond of 2.71 Å, is difficult to be reduced by BHC[41,42]. Hassan et al. reported that hydrazine, which is the main reducing group of BHC, could only reduce the SnO_2 at 300 °C and with the help of hydrogen plasma[43]. We mixed the SnO_2 and BHC and thoroughly milled them. As shown in Fig. 3a, the mixture did not show any colour change after ten days of storage in the glovebox, indicating no black colour SnO or metal Sn have been generated. This confirmed that the generated SnO_2 would not be reduced during device storage. The X-ray photoelectron spectroscopy (XPS) measurement was conducted to investigate the Sn oxidation status on the Sn–Pb perovskite film surface. The binding energy difference between Sn^{4+} and Sn^{2+} can be induced by movement of the Fermi level[44,45]. Therefore, we fit the peak positions consistent with the values we reported on the spin coated NBG perovskites because they have similar chemical environments[37]. The XPS spectra in Fig. 3b unveiled that 15 min air exposure did generate a large amount of Sn^{4+} on the perovskite surface. After storage in the glovebox, the Sn^{4+} peak intensity reduced while Sn^{2+} peak increased, which could attribute to the reduction of Sn^{4+} to Sn^{2+} by BHC. Sn^{4+} peak did not completely disappear even after storage for a month. We assign the left Sn^{4+} signal to be from the remaining SnO_2 on the film surface. In addition, we characterized

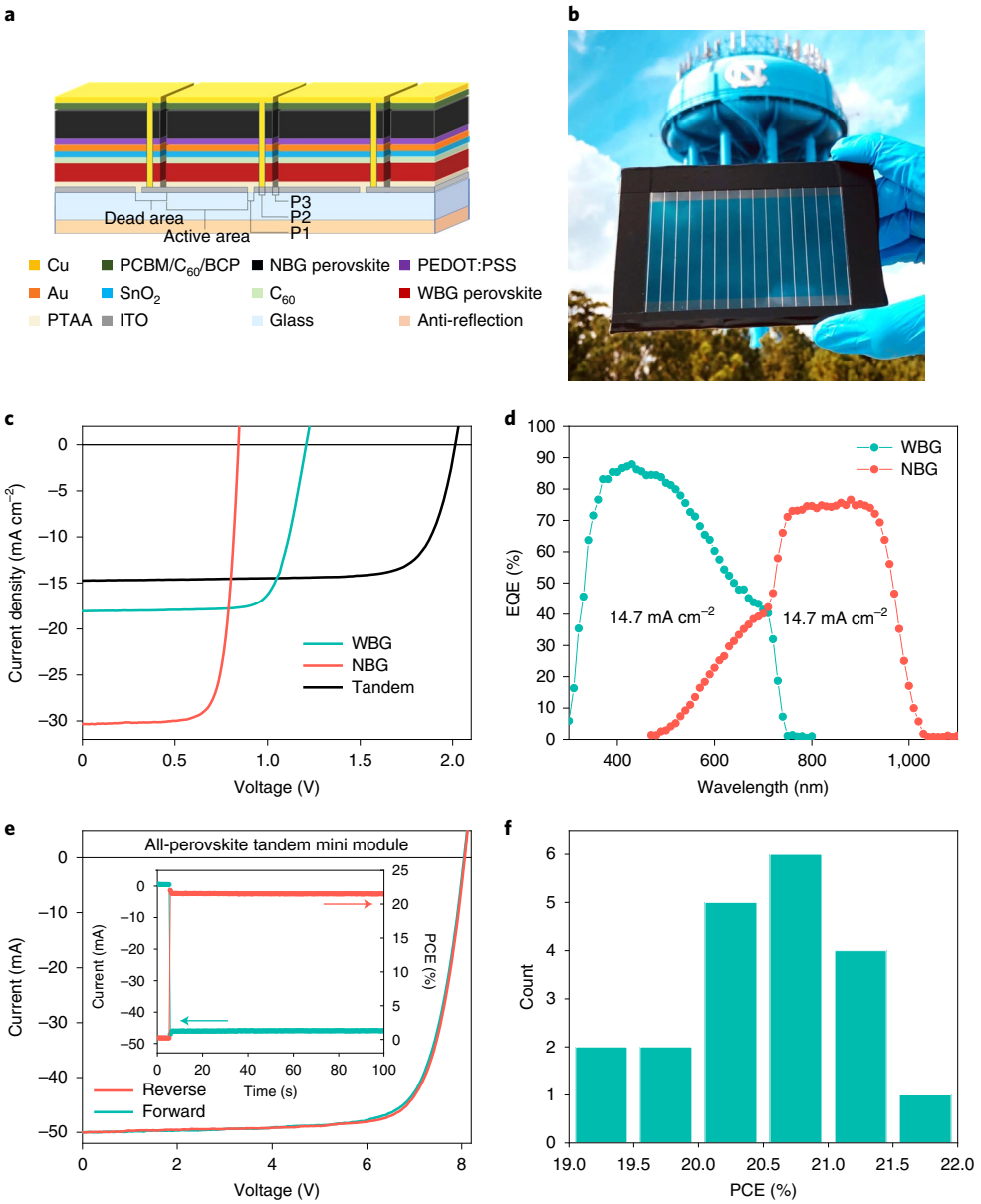

Fig. 4 | All-perovskite tandem solar cell and module performance. a, Schematic structure of the all-perovskite tandem mini module. **b**, Picture of an all-perovskite tandem mini module. **c**, *J*–*V* curves of the single-junction WBG, NBG solar cells and the corresponding tandem solar cell. **d**, EQE spectra of the tandem solar cell with an integrated J_{SC} of 14.7 mA cm^{-2} for both junctions. **e**, *I*–*V* curve of an all-perovskite tandem mini module. The inset shows the stabilized current and power outputs of the champion module fixed at a bias of 6.7 V for 100 s. **f**, Statistic data of 20 all-perovskite tandem mini modules.

the spatial doping-level distribution by drive-level capacitance profiling (DLCP) method[46] for the oxidized NBG perovskite solar cells before and after storage. Supplementary Fig. 14 shows that the high doping concentration at the perovskite film surface caused by oxidation had been dramatically reduced after storage, indicating the reduction of Sn^{4+} by BHC during storage.

On the basis of these results, we summarize the following processes that result in the unusual device efficiency enhancement induced by ageing. During air exposure, the vulnerable NBG perovskite surface degraded into SnO_2, CsI/FAI, SnI_4, iodine and other defects that caused devices' initial degradation. It is noted that although BHC can reduce the oxidation of the precursor solution, this reaction is much slower in solid films. During the storage period, the BHC in the solid film slowly reduced the Sn^{4+} in SnI_4 to Sn^{2+} and reduced iodine into iodide. On the other hand, the remaining SnO_2 is a well-known good electron transporting layer for perovskite devices due to its high electron mobility, excellent chemical compatibility with perovskites and appropriate valence band depth for electron extraction and so on[47,48]. Meanwhile, we have shown that slightly excessive CsI and FAI did not harm the efficiency for $Cs_xFA_{1-x}PbI_3$ perovskites but improved the long stability[6]. This could be the same situation for $Cs_xFA_{1-x}Pb_{0.5}Sn_{0.5}I_3$ perovskites so that the generation of CsI/FAI during oxidation did not reduce device efficiency.

To verify the speculations, transient photovoltage measurement was conducted to evaluate the charge recombination rate change caused by air exposure and ageing. The devices were illuminated by 1 sun light as light bias to introduce a carrier concentration that is comparable to real operation conditions. The results are shown in Fig. 3c–f. Before storage, the devices with air exposure for 1 min already had a longer carrier lifetime of 902 ns than that without air exposure (833 ns), agreeing with the slightly higher efficiency

(Fig. 2c). This could also be caused by the several hours of ageing during top electrode evaporation before testing. Prolonged air exposure increased the non-radiative charge recombination rate, which reduced the carrier lifetime to 814 ns and 634 ns with 5 min and 15 min air exposure, respectively. After storage, all the devices showed an enhanced carrier recombination lifetime, which can be attributed to the reduction of Sn^{4+} and iodine by BHC. The device exposed for 5 min showed the longest carrier recombination lifetime of 1,083 ns after ageing, which agrees well with the champion device PCE achieved at this condition (Fig. 2d). The longer charge recombination lifetime from the devices with optimal air exposure should be caused by the reduced SnI_4 and iodine and the formation of a thin SnO_2 layer on the NBG film surface. However, a 15 min air exposure could induce too much SnI_4 or I_2 so that the BHC in the film might not be enough to remove them, resulting in a shorter carrier recombination lifetime of 828 ns even after storage.

Performance of all-perovskite tandem mini modules

The wide-bandgap perovskite has a composition of $Cs_{0.25}FA_{0.75}Pb(I_{0.85}Br_{0.15})_3$ with 5 mol% $MAPbCl_3$ (ref. [49]). The detailed discussion of the WBG junction can be found in Supplementary Note 5. The tandem cells and mini modules have a stacking of glass/ITO/PTAA/$Cs_{0.25}FA_{0.75}Pb(I_{0.85}Br_{0.15})_3$/$C_{60}$/$SnO_2$/Au/PEDOT:PSS/$Cs_{0.2}FA_{0.8}Pb_{0.5}Sn_{0.5}I_3$/PCBM/$C_{60}$/BCP/Cu, as shown in Fig. 4a, and the picture of an all-perovskite tandem photovoltaic mini module is shown in Fig. 4b. We first went through the whole fabrication process using small area cells. The cross-section SEM image in Supplementary Fig. 17 shows that the thicknesses of the blade-coated NBG and WBG films are 1,000 nm and 233 nm, respectively, which agree with the targeted thicknesses. The 8 mm^2 tandem solar cell showed an efficiency of 23.1% with V_{OC} of 2.01 V, J_{SC} of 14.8 mA cm^{-2} and FF of 77.5%. (Fig. 4c and Supplementary Table 6). The EQE spectra of the WBG and NBG junctions give an integrated J_{SC} of 14.7 mA cm^{-2} (Fig. 4d), which is well balanced and close to the J_{SC} from the J–V measurement. In fabricating a mini module with an area of 10–20 cm^2, the total scribing time for P2 and P3 lines (Fig. 4a) was around 20 min. The additional layers covering the NBG films should extend the operation window in air to be longer than the optimal 5 min shown above. The encapsulated mini modules were stored in a glovebox for two days to reduce the Sn^{4+} and iodine before measurement. Figure 4e (Supplementary Table 7) shows current–voltage (I–V) performance of a champion mini module with four subcells and an aperture area of 14.3 cm^2, giving an aperture PCE of 21.6% with negligible hysteresis. The stabilized photocurrent of the module at maximum power output point is shown as an inset of Fig. 4e, giving a stabilized PCE of 21.5%. Each subcell in the mini module has a width of 0.65 cm, in which the dead area is 0.04 cm wide measured by optical microscopy (Supplementary Fig. 18), corresponding to a geometry filling factor of 93.8%. Therefore, the active area PCE of the tandem mini module is 23.0%. Even though the module active area PCE is very close to that of small cell PCE of 23.0%, there was still a cell-to-module loss which was compensated by the anti-reflection layer on modules. The cell-to-module derate of only 6.5% (from 23.1% on small cells to 21.6% on modules) is much smaller than that of 18.2% on the record-reported single-junction perovskite module[10]. The low cell-to-module derate attributed to lower photocurrent, and higher photovoltage reduced the resistive loss by 66% based on our analysis shown in Supplementary Note 6. The average V_{OC} for each subcell is 2.01 V, which is the same as that of the small devices. The no loss of V_{OC} from cell-to-module transition indicates the 20 min air exposure during scribing, and other processes did not damage the NBG perovskite films. The reduced FF could stem from the large subcell area, increasing the series resistance to 48.3 Ω cm^2, which is around five times of the 8 mm^2 small cells. The efficiency statistics of 20 all-perovskite tandem mini modules are listed in Fig. 4f, showing that the average aperture efficiency of the tandem modules reached 20.5%. Supplementary Fig. 19 shows the long-term photo stability of the all-perovskite tandem solar module under 1 sun illumination. The module retained ~90.0% of its initial PCE after 250 h.

Conclusions

In summary, we adopted a hot gas-assisted blade-coating strategy to deposit high-quality, large-area and thick NBG perovskite films to fabricate all-perovskite tandem modules. The reductant BHC prevented the formation of Sn^{4+} during film fabrication and also reduced the Sn^{4+} and iodine generated during air exposure. We demonstrate a performance-enhancement mechanism on Sn–Pb perovskite solar cells resulting from a combination of oxidation, BHC in perovskites and a post-fabrication storage process that makes modules efficient. The all-perovskite tandem mini modules have been fabricated and achieved a PCE of 21.6% with an aperture area of 14.3 cm^2.

Methods

Materials. Lead iodide (PbI_2, 99.999% trace metals), tin(ii) iodide (SnI_2, 99.999%), lead(ii) bromide ($PbBr_2$, 99.999%), lead(ii) chloride ($PbBr_2$, 99.999%), tin(ii) fluoride (SnF_2, 99%), caesium iodide (CsI, 99.999%), Poly[bis(4-phenyl)(2,4,6-trimethylphenyl)amine] (PTAA), bathocuproine (BCP), anhydrous N,N-dimethylformamide (DMF, 99.8%), anhydrous dimethyl sulfoxide (DMSO, ≥ 99.9%), anhydrous acetonitrile (99.8%), anhydrous 2-Propanol (IPA, 99.5%), L-α-phosphatidylcholine (LP), propylhydrazine hydrochloride, (2-thienylmethyl)hydrazine hydrochloride, hydrazine monohydrochloride and anhydrous toluene (99.8%) were purchased from Sigma-Aldrich and used without further purification. Methylammonium iodide, formamidinium iodide (FAI) and phenethylammonium iodide (PEAI) were purchased from Greatcell Solar. C_{60} and [6,6]-phenyl-C61-butyric acid methyl ester (PCBM) were purchased from Nano-C. Poly(3,4-ethylenedioxythiophene):poly(styrene sulfonate) PEDOT:PSS (Clevios P VP AI 4083) was purchased from Heraeus. Benzylhydrazine hydrochloride (BHC, 95%) was purchased from AmBeed.

Perovskite precursor solution preparation. For the WBG perovskite, 1.35 M $Cs_{0.25}FA_{0.75}Pb(I_{0.85}Br_{0.15})_3$ precursor solution was prepared in mixed solvents of DMF and DMSO with a volume ratio of 16:1. The molar ratios for CsI:FAI and PbI_2:$PbBr_2$ were 0.25:0.75 and 0.775:0.225, respectively. The precursor solution was stirred at room temperature for 1 h. In addition, 5 mol% (relative to 1.35 M precursor solution) $MAPbCl_3$, 0.68 mg ml^{-1} PEAI, 0.68 mg ml^{-1} BHC, 0.17 mg ml^{-1} LP and 0.17 mg ml^{-1} FAH_2PO_2 were added in the solution before blade coating.

For the NBG perovskite 2.4 M $Cs_{0.2}FA_{0.8}Pb_{0.5}Sn_{0.5}I_3$ precursor solution was prepared in mixed solvents of DMF and DMSO with a volume ratio of 43:7. The molar ratios for CsI:FAI and PbI_2:SnI_2 were 0.2:0.8 and 0.5:0.5, respectively. In addition, 10 mol% (relative to SnI_2) SnF_2 was added in the precursor solution. The precursor solution was stirred at room temperature for 3 h. The additives 1 mg ml^{-1} PEAI and 1 mg ml^{-1} BHC were added into the precursor solution before blade coating. In addition, 20 vol% (relative to precursor solution) acetonitrile was added before blade coating to dilute the solution.

Device fabrication. The commercial patterned ITO substrates were cleaned by ultrasonication with deionized water, acetone and isopropanol sequentially. The dried substrate was then subjected to UV–ozone treatment for 15 min.

Single-junction WBG perovskite solar cell fabrication. PTAA (2 mg ml^{-1}) dissolved in toluene was blade coated on the substrates without gas-assisted drying. The coating was conducted in ambient air (20 ± 1 °C, 65 ± 5 RH%). The coating speed was 20 mm s^{-1}. The coating gap between the blade and substrates was 150 μm. Subsequently, the $Cs_{0.25}FA_{0.75}Pb(I_{0.85}Br_{0.15})_3$ (with 5 mol% $MAPbCl_3$) precursor solution was blade coated in a glovebox with room temperature N_2 gas-assisted drying. The coating speed was 20 mm s^{-1} with a coating gap of 215 μm. The as-coated films annealed on one hot plate at 130 °C for 10 s, then transferred to another hot plate with 100 °C to anneal another 15 min. The perovskite film thickness was around 230 nm. Finally, 25 nm C_{60}, 6 nm BCP and 80 nm Cu were thermal evaporated subsequently onto the samples.

Single-junction NBG perovskite solar cell fabrication. Commercial PEDOT:PSS was blade coated on the substrates heated to 70 °C. The coating was conducted in ambient air (20 ± 1 °C, 65 ± 5 RH%). The coating speed was 20 mm s^{-1} with a coating gap of 200 μm. The blade-coated films annealed at 130 °C for 10 min. Subsequently, the $Cs_{0.2}FA_{0.8}Pb_{0.5}Sn_{0.5}I_3$ precursor solution was blade coated in a glovebox under blowing N_2 gas at 100 °C. The gas temperature was controlled by a proportional–integral–derivative controller through a thermocouple integrated on the in-line heater. The coating speed was 25 mm s^{-1} with a coating gap of 275 μm. The as-coated films annealed on one hot plate at 150 °C for 10 s, then transferred to

another hot plate with 100 °C to anneal another 7 min. The perovskite film thickness was around 1,000 nm. Subsequently, the film surface was treated with BHC in a glovebox by spin coating a 1 mg ml^{-1} BHC solution in IPA at 5,000 r.p.m. for 25 s. PCBM dissolved in toluene (10 mg ml^{-1}) was spin coated at 5,000 r.p.m. for 25 s. After annealing on a hot plate at 70 °C for 10 min, the samples were exposed in air (20 ± 1 °C, 65 ± 5 RH%) for 1 min, 5 min and 15 min, respectively. Finally, 25 nm C_{60}, 6 nm BCP and 80 nm Cu were subsequently thermally evaporated onto the samples.

Fabrication of tandem solar cells and modules. PTAA (2 mg ml^{-1}) dissolved in toluene was blade coated on the substrates without gas-assisted drying. The coating was conducted in ambient air (20 ± 1 °C, 65 ± 5 RH%). The coating speed was 20 mm s^{-1}. The coating gap between the blade and substrates was 150 µm. Subsequently, the $Cs_{0.25}FA_{0.75}Pb(I_{0.85}Br_{0.15})_3$ (with 5 mol% $MAPbCl_3$) precursor solution was blade coated in a glovebox with room temperature N_2 gas-assisted drying. The coating speed was 20 mm s^{-1} with a coating gap of 215 µm. The as-coated films annealed on one hot plate at 130 °C for 10 s, then transferred to another hot plate with 100 °C to anneal another 15 min. After thermal evaporation of 25 nm C_{60} on the WBG films, the samples were transferred to an atomic layer deposition (Veeco Savannah S200) chamber to deposit 20 nm SnO_2 using precursors of tetrakis(dimethylamino) tin(iv) (99.9999%) and deionized water. Subsequently, 1 nm Au was thermally evaporated onto the samples. PEDOT:PSS was blade coated onto the samples in ambient air (20 ± 1 °C, 65 ± 5 RH%) heated to 70 °C. The coating speed was 20 mm s^{-1} with a coating gap of 200 µm. The films annealed at 100 °C for 10 min in a glovebox. The $Cs_{0.2}FA_{0.8}Pb_{0.5}Sn_{0.5}I_3$ precursor solution was blade coated in a glovebox under blowing N_2 gas at 100 °C. The coating speed was 25 mm s^{-1} with a coating gap of 275 µm. The as-coated films annealed on one hot plate at 150 °C for 10 s, then transferred to another hot plate with 100 °C to anneal another 7 min. Subsequently, the film surface was treated with BHC by spin coating a 1 mg ml^{-1} BHC solution in IPA at 5,000 r.p.m. for 25 s in a glovebox. PCBM dissolved in toluene (10 mg ml^{-1}) was spin coated at 5,000 r.p.m. for 25 s in a glovebox. And samples annealed on a hot plate at 70 °C for 10 min. For small cells, the samples were exposed in air (20 ± 1 °C, 65 ± 5 RH%) for 5 min before 25 nm C_{60}, 6 nm BCP and 80 nm Cu were subsequently thermally evaporated to complete the fabrication. For modules, 25 nm C_{60}, 6 nm BCP and 20 nm Cu were subsequently thermally evaporated. The samples were then transferred to air (20 ± 1 °C, 65 ± 5 RH%) to laser scribe P2 lines. After scribing, another layer of 180 nm Cu was deposited by thermal evaporation. The samples were scribed P3 lines with laser in air (20 ± 1 °C, 65 ± 5 RH%) to complete the module fabrication. All the devices were encapsulated in a glovebox with epoxy and glass on top. The devices were stored in the glovebox before measurement. In addition, polydimethylsiloxane anti-reflection layers were applied for *J*–*V* measurements.

Device characterizations. The current–voltage measurements were performed under the simulated AM 1.5 G irradiation produced by a Xenon-lamp-based solar simulator (Oriel 94043 A, Class AAA Solar Simulator). The light intensity was calibrated using a silicon reference cell with a KG5 glass filter (Newport 91150-KG5). The data were recorded by a Keithley 2400 Source-Meter. All the *J*–*V* measurements were taken under 100 mW cm^{-2} illumination at a scan rate of 0.1 V s^{-1} with a delay time of 10 ms, and there was no preconditioning before measurements. EQE spectra were measured on a Newport quantum efficiency measurement kit by focusing a monochromatic beam from a Bruker Vertex 80 v Fourier transform interferometer with tungsten lamp source onto the devices. The photocurrent was recorded by a Stanford Research Systems SR570 current preamplifier. The calibration was done on a Newport silicon reference solar cell with a known EQE. Blue (~470 nm) and infrared (~940 nm) light bias with an intensity of ~0.3 sun was applied to measure the EQE of the NBG and WBG junctions, respectively. Scanning electron microscope images were taken on FEI Helios 600 NanoLab DualBeam System operating at 5 kV. The XRD pattern was obtained with a Rigaku sixth generation MiniFlex X-ray diffractometer. Ultraviolet–visible–near-infrared absorbance was characterized by PerkinElmer LAMBDA 1050 spectrophotometers equipped with an integrating sphere. The high-resolution XPS measurements were conducted with a monochromatic Al Kα source (1,486.6 eV). The samples were placed in an ultra-high vacuum analytical chamber under a base pressure of 1×10^{-10} Torr. The X-ray gun was running at 10 kV and 20 mA with a spot size of 0.6 mm in diameter on the sample. Transient photovoltage data was collected by an oscilloscope (DSO-X 3104 A, KEYSIGHT) with internal impedance of 1 MΩ. The solar devices were applied a 1 sun light bias. A 337 nm laser pulse (Stanford Research Systems NL 100 nitrogen laser, frequency of 10 Hz and pulse width of <3.5 ns) hit on the device to trigger a photovoltage variation (<5% of V_{OC}) onto the V_{OC}. DLCP was characterized using an Agilent E4980A precision inductance–capacitance–resistance (LCR) meter. The voltage was scanning from 0 V to the V_{OC} of the perovskite solar cells. The a.c. frequency was set to be 1,000 kHz to characterize the doping level. For the long-term stability measurement, the devices that encapsulated with epoxy and glass were connected to resistors to operate at their maximum power point at the beginning of the test. The devices were put in air (relative humidity of 30–65%) under constant illumination provided by a light-emitting diode (LED) light source with an intensity of 1 sun. The temperature of the devices was kept at ~30 °C. The devices were scanned *I*–*V* curves every 48 h.

Reporting summary. Further information on research design is available in the Nature Research Reporting Summary linked to this article.

Data availability

All data generated or analysed during this study are included in the published article and its Supplementary Information and source data files. Source data are provided with this paper.

Received: 17 November 2021; Accepted: 25 July 2022;
Published online: 29 August 2022

References

1. Leijtens, T., Bush, K. A., Prasanna, R. & McGehee, M. D. Opportunities and challenges for tandem solar cells using metal halide perovskite semiconductors. *Nat. Energy* **3**, 828–838 (2018).
2. Dai, X. et al. Pathways to high efficiency perovskite monolithic solar modules. *PRX Energy* **1**, 013004 (2022).
3. Heo, J. H. & Im, S. H. $CH_3NH_3PbBr_3$–$CH_3NH_3PbI_3$ perovskite–perovskite tandem solar cells with exceeding 2.2 V open circuit voltage. *Adv. Mater.* **28**, 5121–5125 (2016).
4. Lin, R. et al. All-perovskite tandem solar cells with improved grain surface passivation. *Nature* **603**, 73–78 (2022).
5. Green, M. A. et al. Solar cell efficiency tables (version 58). *Prog. Photovoltaics Res. Appl.* **29**, 657–667 (2021).
6. Deng, Y. et al. Defect compensation in formamidinium–caesium perovskites for highly efficient solar mini-modules with improved photostability. *Nat. Energy* **6**, 633–641 (2021).
7. Chen, S., Xiao, X., Gu, H. & Huang, J. Iodine reduction for reproducible and high-performance perovskite solar cells and modules. *Sci. Adv.* **7**, eabe8130 (2021).
8. Deng, Y. et al. Reduced self-doping of perovskites induced by short annealing for efficient solar modules. *Joule* **4**, 1949–1960 (2020).
9. Deng, Y. et al. Tailoring solvent coordination for high-speed, room-temperature blading of perovskite photovoltaic films. *Sci. Adv.* **5**, eaax7537 (2019).
10. Chen, S. et al. Stabilizing perovskite–substrate interfaces for high-performance perovskite modules. *Science* **373**, 902–907 (2021).
11. Yang, Z. et al. Enhancing electron diffusion length in narrow-bandgap perovskites for efficient monolithic perovskite tandem solar cells. *Nat. Commun.* **10**, 4498 (2019).
12. Xiao, K. et al. All-perovskite tandem solar cells with 24.2% certified efficiency and area over 1 cm^2 using surface-anchoring zwitterionic antioxidant. *Nat. Energy* **5**, 870–880 (2020).
13. Deng, Y. et al. Surfactant-controlled ink drying enables high-speed deposition of perovskite films for efficient photovoltaic modules. *Nat. Energy* **3**, 560–566 (2018).
14. Lin, R. et al. Monolithic all-perovskite tandem solar cells with 24.8% efficiency exploiting comproportionation to suppress Sn (ii) oxidation in precursor ink. *Nat. Energy* **4**, 864–873 (2019).
15. Nakamura, T. et al. Sn (IV)-free tin perovskite films realized by in situ Sn (0) nanoparticle treatment of the precursor solution. *Nat. Commun.* **11**, 3008 (2020).
16. He, X. et al. Highly efficient tin perovskite solar cells achieved in a wide oxygen concentration range. *J. Mater. Chem. A* **8**, 2760–2768 (2020).
17. Kayesh, M. E. et al. Enhanced photovoltaic performance of $FASnI_3$-based perovskite solar cells with hydrazinium chloride coadditive. *ACS Energy Lett.* **3**, 1584–1589 (2018).
18. Tai, Q. et al. Antioxidant grain passivation for air-stable tin-based perovskite solar cells. *Angew. Chem. Int. Ed.* **58**, 806–810 (2019).
19. Cao, J. et al. Enhanced performance of tin-based perovskite solar cells induced by an ammonium hypophosphite additive. *J. Mater. Chem. A* **7**, 26580–26585 (2019).
20. Meng, X. et al. Highly reproducible and efficient $FASnI_3$ perovskite solar cells fabricated with volatilizable reducing solvent. *J. Phys. Chem. Lett.* **11**, 2965–2971 (2020).
21. Park, N.-G. & Zhu, K. Scalable fabrication and coating methods for perovskite solar cells and solar modules. *Nat. Rev. Mater.* **5**, 333–350 (2020).
22. Mali, S. S., Patil, J. V. & Hong, C. K. Hot-air-assisted fully air-processed barium incorporated $CsPbI_2Br$ perovskite thin films for highly efficient and stable all-inorganic perovskite solar cells. *Nano Lett.* **19**, 6213–6220 (2019).
23. Su, J. et al. Efficient perovskite solar cells prepared by hot air blowing to ultrasonic spraying in ambient air. *ACS Appl. Mater. Interfaces* **11**, 10689–10696 (2019).
24. Hu, Q. et al. In situ dynamic observations of perovskite crystallisation and microstructure evolution intermediated from $[PbI_6]^{4-}$ cage nanoparticles. *Nat. Commun.* **8**, 15688 (2017).
25. Yang, M. et al. Perovskite ink with wide processing window for scalable high-efficiency solar cells. *Nat. Energy* **2**, 17038 (2017).

26. Yang, Z. et al. Slot-die coating large-area formamidinium–cesium perovskite film for efficient and stable parallel solar module. *Sci. Adv.* **7**, eabg3749 (2021).
27. Li, N. et al. Liquid medium annealing for fabricating durable perovskite solar cells with improved reproducibility. *Science* **373**, 561–567 (2021).
28. Chen, S. et al. Crystallization in one-step solution deposition of perovskite films: upward or downward? *Sci. Adv.* **7**, eabb2412 (2021).
29. Chen, B. et al. Blade-coated perovskites on textured silicon for 26%-efficient monolithic perovskite/silicon tandem solar cells. *Joule* **4**, 850–864 (2020).
30. Pascual, J. et al. Origin of Sn (ii) oxidation in tin halide perovskites. *Mater. Adv.* **1**, 1066–1070 (2020).
31. Moghadamzadeh, S. et al. Spontaneous enhancement of the stable power conversion efficiency in perovskite solar cells. *J. Mater. Chem. A* **8**, 670–682 (2020).
32. Tsai, H. et al. Light-induced lattice expansion leads to high-efficiency perovskite solar cells. *Science* **360**, 67–70 (2018).
33. Qiu, W. et al. High efficiency perovskite solar cells using a PCBM/ZnO double electron transport layer and a short air-aging step. *Org. Electron.* **26**, 30–35 (2015).
34. DeQuilettes, D. W. et al. Photo-induced halide redistribution in organic–inorganic perovskite films. *Nat. Commun.* **7**, 11683 (2016).
35. Mosconi, E., Meggiolaro, D., Snaith, H. J., Stranks, S. D. & De Angelis, F. Light-induced annihilation of Frenkel defects in organo-lead halide perovskites. *Energy Environ. Sci.* **9**, 3180–3187 (2016).
36. Bi, C., Zheng, X., Chen, B., Wei, H. & Huang, J. Spontaneous passivation of hybrid perovskite by sodium ions from glass substrates: mysterious enhancement of device efficiency revealed. *ACS Energy Lett.* **2**, 1400–1406 (2017).
37. Yu, Z. et al. Simplified interconnection structure based on C_{60}/SnO_{2-x} for all-perovskite tandem solar cells. *Nat. Energy* **5**, 657–665 (2020).
38. Lanzetta, L. et al. Degradation mechanism of hybrid tin-based perovskite solar cells and the critical role of tin (IV) iodide. *Nat. Commun.* **12**, 2853 (2021).
39. Leijtens, T., Prasanna, R., Gold-Parker, A., Toney, M. F. & McGehee, M. D. Mechanism of tin oxidation and stabilization by lead substitution in tin halide perovskites. *ACS Energy Lett.* **2**, 2159–2165 (2017).
40. Zhou, Y., Poli, I., Meggiolaro, D., De Angelis, F. & Petrozza, A. Defect activity in metal halide perovskites with wide and narrow bandgap. *Nat. Rev. Mater.* **6**, 986–1002 (2021).
41. Project, T. M. *Materials Data on SnI_4 by Materials Project; Lawrence Berkeley National Lab* (LBNL Materials Project, 2020).
42. Project, T. M. *Materials Data on SnO_2 by Materials Project; Lawrence Berkeley National Lab* (LBNL Materials Project, 2020).
43. Abdollahi, H., Samkan, M., Mohajerzadeh, M. A., Sanaee, Z. & Mohajerzadeh, S. High-performance tin-oxide supercapacitors using hydrazine functionalising assisted by hydrogen plasma treatment. *Micro Nano Lett.* **14**, 1268–1273 (2019).
44. Yang, C. et al. Observation of an intermediate band in Sn-doped chalcopyrites with wide-spectrum solar response. *Sci. Rep.* **3**, 1286 (2013).
45. Pujilaksono, B. et al. X-ray photoelectron spectroscopy studies of indium tin oxide nanocrystalline powder. *Mater. Charact.* **54**, 1–7 (2005).
46. Ni, Z. et al. Resolving spatial and energetic distributions of trap states in metal halide perovskite solar cells. *Science* **367**, 1352–1358 (2020).
47. Jiang, Q., Zhang, X. & You, J. SnO_2: a wonderful electron transport layer for perovskite solar cells. *Small* **14**, 1801154 (2018).
48. Xiong, L. et al. Review on the application of SnO_2 in perovskite solar cells. *Adv. Funct. Mater.* **28**, 1802757 (2018).
49. Xu, J. et al. Triple-halide wide–band gap perovskites with suppressed phase segregation for efficient tandems. *Science* **367**, 1097–1104 (2020).

Acknowledgements

This material and device development was mainly supported by Defense Threat Reduction Agency under grant HDTRA1-19-1-0024. We thank the financial support from National Science Foundation under award DMR-1903981 and ECCS-1542015 for material characterizations. The device characterization was supported in part by the Solar Energy Technologies office within the US Department of Energy, Office of Energy Efficiency and Renewable Energy, under award number DE-EE0008749. The content of the information does not necessarily reflect the position or the policy of the federal government, and no official endorsement should be inferred.

Author contributions

J.H. conceived the project. X.D. designed the experiments and conducted the device fabrication and most of the characterizations. S.C. helped in introducing the reduction agent. K.W. and Y.G. performed the XPS measurements. H.J. and L.Z. conducted the XRD measurement. Z.N. helped on the DLCP characterization. Z.Y. contributed to the composition of NBG perovskite. B.C. helped on the long-term stability tests. X.D. and J.H. wrote the paper, and all authors reviewed the paper.

Competing interests

The authors declare no competing interests.

Additional information

Supplementary information The online version contains supplementary material available at https://doi.org/10.1038/s41560-022-01102-w.

Correspondence and requests for materials should be addressed to Jinsong Huang.

Peer review information *Nature Energy* thanks Shuzi Hayase and the other, anonymous, reviewer(s) for their contribution to the peer review of this work.

Reprints and permissions information is available at www.nature.com/reprints.

Publisher's note Springer Nature remains neutral with regard to jurisdictional claims in published maps and institutional affiliations.

nature research

Corresponding author(s): Jinsong Huang

Solar Cells Reporting Summary

Nature Research wishes to improve the reproducibility of the work that we publish. This form is intended for publication with all accepted papers reporting the characterization of photovoltaic devices and provides structure for consistency and transparency in reporting. Some list items might not apply to an individual manuscript, but all fields must be completed for clarity.

For further information on Nature Research policies, including our data availability policy, see Authors & Referees.

Experimental design

Please check: are the following details reported in the manuscript?

1. Dimensions

Area of the tested solar cells	☒ Yes ☐ No	8 mm2 for solar cells and 14.3 cm2 for mini-modules.
Method used to determine the device area	☒ Yes ☐ No	Supplementary Fig. 18; "Device characterizations" section.

2. Current-voltage characterization

Current density-voltage (J-V) plots in both forward and backward direction	☒ Yes ☐ No	Fig. 2B, Fig. 4E.
Voltage scan conditions *For instance: scan direction, speed, dwell times*	☒ Yes ☐ No	"Device characterizations" section.
Test environment *For instance: characterization temperature, in air or in glove box*	☒ Yes ☐ No	"Device characterizations" section.
Protocol for preconditioning of the device before its characterization	☐ Yes ☒ No	No preconditioning is required before characterization.
Stability of the J-V characteristic *Verified with time evolution of the maximum power point or with the photocurrent at maximum power point; see ref. 7 for details.*	☒ Yes ☐ No	Fig. 4E.

3. Hysteresis or any other unusual behaviour

Description of the unusual behaviour observed during the characterization	☒ Yes ☐ No	Very minor hysteresis was observed.
Related experimental data	☒ Yes ☐ No	Fig. 2B, Fig. 4E.

4. Efficiency

External quantum efficiency (EQE) or incident photons to current efficiency (IPCE)	☒ Yes ☐ No	Fig. 4D.
A comparison between the integrated response under the standard reference spectrum and the response measure under the simulator	☒ Yes ☐ No	"Performance of all-perovskite tandem mini-modules" section in main text.
For tandem solar cells, the bias illumination and bias voltage used for each subcell	☒ Yes ☐ No	"Device characterizations" section..

5. Calibration

Light source and reference cell or sensor used for the characterization	☒ Yes ☐ No	"Device characterizations" section.
Confirmation that the reference cell was calibrated and certified	☒ Yes ☐ No	"Device characterizations" section.

Calculation of spectral mismatch between the reference cell and the devices under test	☒ Yes ☐ No	A best AAA Solar Simulator in UNC is used for JV measurement. A dual-lamp solar simulator with a Xe lamp and a halogen lamp, which allows independent control of blue and near-infrared illumination in ASU is used for verify the JV results of the tandem cells tested in UNC. The spectral mismatch of the dual-lamp solar simulator are < 5% according to JIS-C-8942 from 400 nm to 1100 nm with a 50 nm interval, and < 7% from 350 nm to 400 nm.

6. Mask/aperture

Size of the mask/aperture used during testing	☒ Yes ☐ No	"Performance of all-perovskite tandem mini-modules" section in main text.
Variation of the measured short-circuit current density with the mask/aperture area	☐ Yes ☒ No	The aperture area is fixed for each device.

7. Performance certification

Identity of the independent certification laboratory that confirmed the photovoltaic performance	☐ Yes ☒ No	No certification is conducted in this work since the no record efficiency is reported. Our current work focuses on how to scale up the manufacturing of all-perovskite tandem solar modules. The novel scalable strategy and the anti-oxidation approach are the highlights of this work.
A copy of any certificate(s) *Provide in Supplementary Information*	☐ Yes ☒ No	No certification is conducted in this work.

8. Statistics

Number of solar cells tested	☒ Yes ☐ No	Fig. 4F.
Statistical analysis of the device performance	☒ Yes ☐ No	Fig. 4F; "Performance of all-perovskite tandem mini-modules" section in main text.

9. Long-term stability analysis

Type of analysis, bias conditions and environmental conditions *For instance: illumination type, temperature, atmosphere humidity, encapsulation method, preconditioning temperature*	☒ Yes ☐ No	Supplementary Fig. 7 and Supplementary Fig. 19.